Supporting Information

Superior Thermoelectric Performance in PbTe-PbS Pseudo-binary: Extremely Low Thermal Conductivity and Modulated Carrier Concentration

Di Wu, [1,6,#] Li-Dong Zhao, [2,3] Xiao Tong, [1,#] Wei Li, [1,6] Lijun Wu, [4] Qing Tan, [5] Yanling Pei, [2] Li Huang, [1,6] Jing-Feng Li, [5] Yimei Zhu, [4] Mercouri G. Kanatzidis[3,*] and Jiaqing He[1,6,*]

[1]Department of Physics, South University of Science and Technology of China, Shenzhen 518055, China

[2]School of Materials Science and Engineering, Beihang University, Beijing 100191, China

[3]Department of Chemistry, Northwestern University, Evanston, Illinois 60208, USA

[4]Condensed Matter Physics and Materials Science Department, Brookhaven National Laboratory, Upton 11973, USA

[5]Key Laboratory of New Ceramics and Fine Processing, School of Materials Science and Eng ineering, Tsinghua University, Beijing, 100084, China

[6]Shenzhen Key Laboratory of Thermoelectric Materials, Shenzhen, 518055, China

[#]These authors contributed equally to this work
[*] To whom correspondence should be addressed.
Email: he.jq@sustc.edu.cn, m-kanatzidis@northwestern.edu

Additional thermal and electrical properties

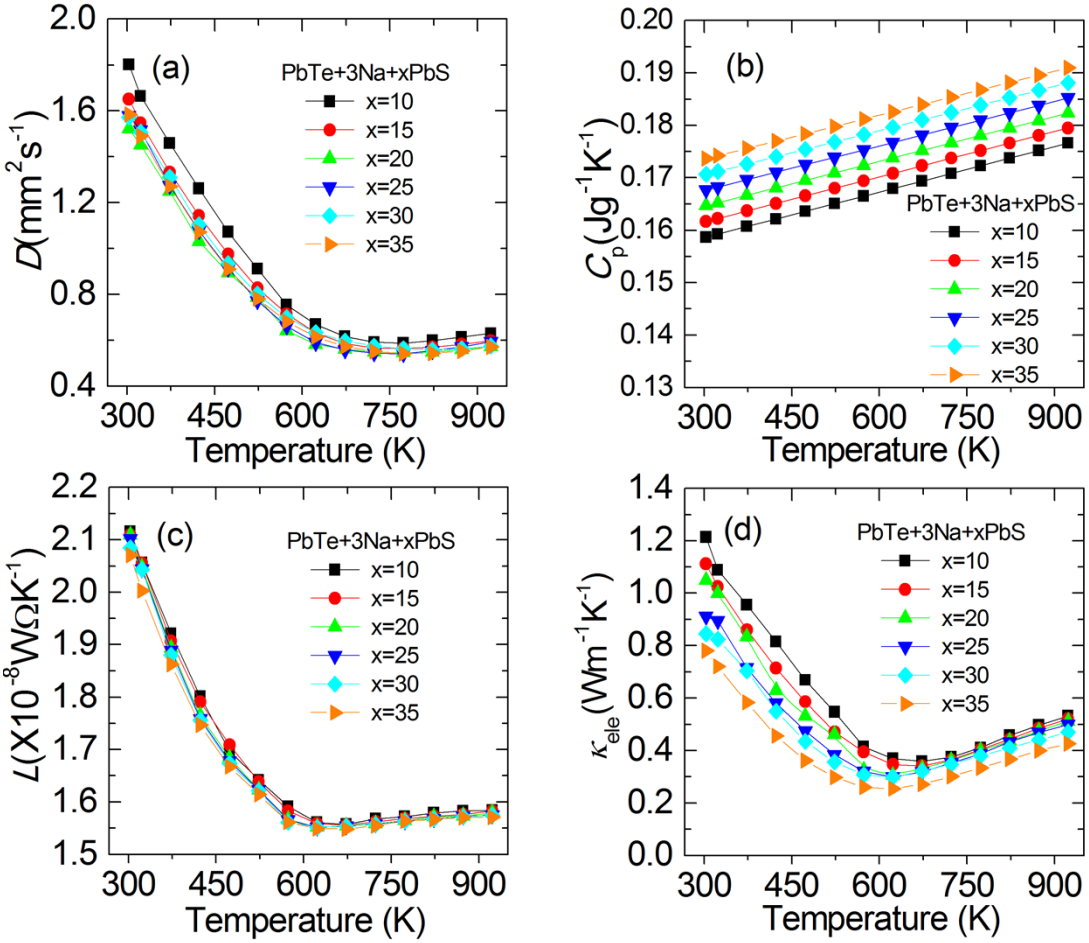

Figure S1 (a) Thermal diffusivities, (b) specific heat capacities, (c) *Lorenz* numbers, (d) electrical thermal conductivities of 3 at% Na-doped $PbTe_{1-x}S_x$ composites with x=10%, 15%, 20%, 25%, 30% and 35% respectively.

The mass densities of nominal compositions of $(PbTe)_{1-x}(PbS)_x$-3 at% Na (x = 10%, 15%, 20%, 25%, 30% and 35%) were measured to be 8.16, 8.13, 8.10, 8.07, 8.03 and 8.00 g cm^{-3}, respectively.

Powdery X-Ray Diffraction and Scanning Electron Microscopy

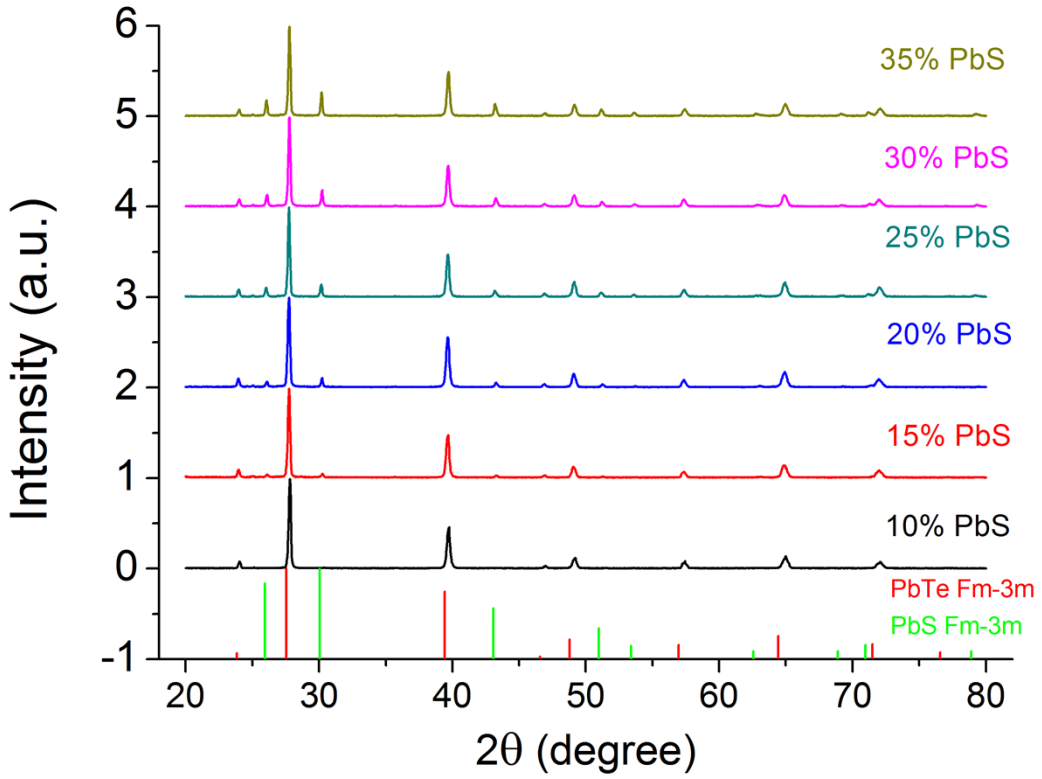

Figure S2 Powder X-Ray Diffraction patterns of 3% Na doped PbTe-xPbS with *x* increasing from 10% to 35%. It is clearly seen that the characteristic peak intensities of PbS phase increase with *x*.

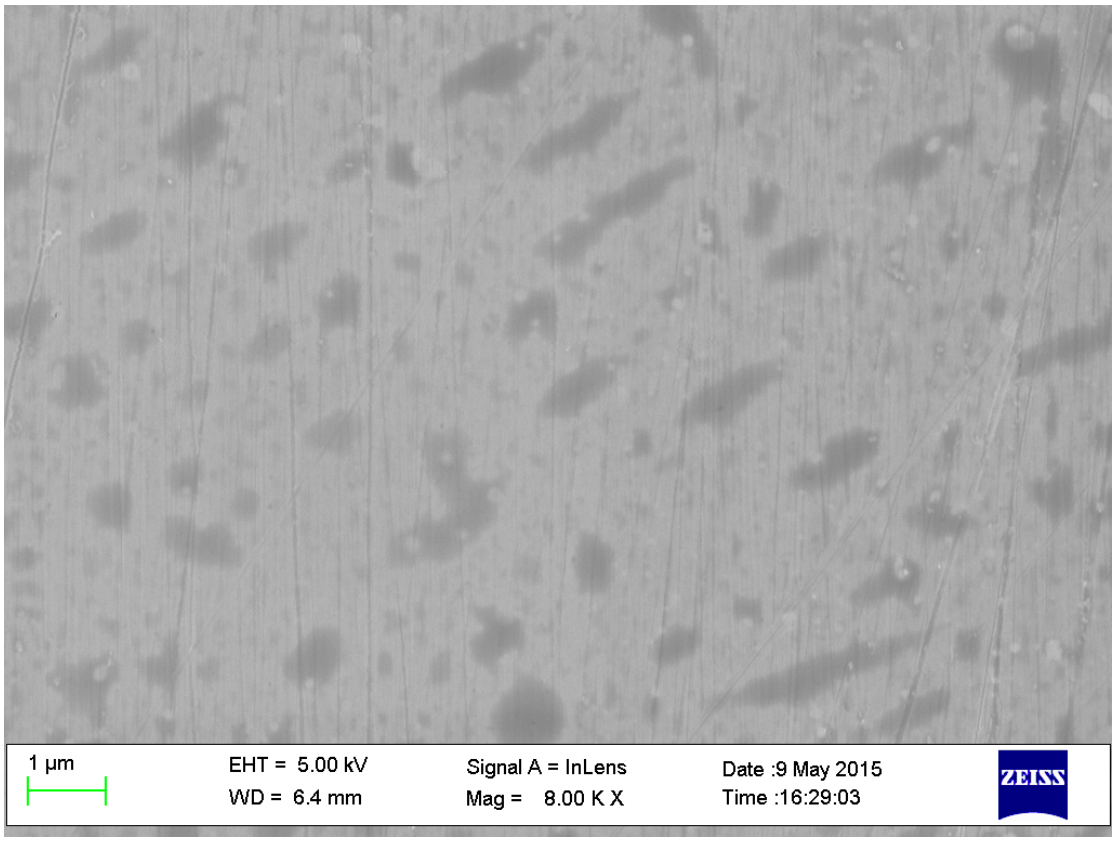

Figure S3 Scanning Electron Microscopy of 3% Na doped PbTe-20%PbS. It is seen that

secondary (PbS) phase (nanoscale and mesoscale) spread homogeneously all over the sample.

SEM images of 20% PbS alloyed PbTe clearly illustrate the coexistence of both nanoscale precipitates of secondary phase (PbS) and larger ones in mesoscale, which provide hierarchical architectures to effectively scatter phonons of the whole spectrum when combined with dissolved PbS point defects. As for the composition of $(PbTe)_{0.9}(PbS)_{0.1}$, the matrix and the nanoprecipitates are believed, respectively, to be sulfur-poor and sulfur-rich; however, as evidenced from TEM observations in **Figure 2** and **3**, the composition difference between them is small (even XRD cannot detect the precipitated PbS phase). The small composition contrast implies their inefficiency in phonon scattering despite the precipitates' small size and high number density.

Density Functional Theory calculations

The first-principles DFT calculations were performed using the standard frozen-core projector augmented-wave (PAW) method as implemented in VASP code. The exchange-correlation effects were treated with the generalized gradient approximation (GGA) was described by the Perdew-Burke-Ernzerh of gradient-corrected functions[1-4]. The Kohn-Sham orbitals were expanded in plane waves with an energy cutoff of 300 eV. Spin-orbit interaction (SOI) was included to account for the relativistic effects. The calculated lattice constants of NaCl-type PbTe and PbS were 6.57Å and 6.01Å, respectively, in good agreement with the experimental values. A 2 × 2 × 2 supercell with 64 atoms is used to model the bulk PbTe and PbS systems. A Monkhorst-Pack Γ-centered 5 × 5 × 5 k-point mesh was used for Brillouin zone sampling. Optimized atomic geometries were obtained by conjugate gradient minimization when the Hellman-Feynman forces on all atoms are below 0.01 eV/Å, without imposing any symmetry constraint.

The formation energy, E_{form}, describing the relative difficulty for different point defects is a widely accepted gauge of energetic stability. The formation energy in the q charge state is defined by

$$E_{form} = E(\text{defect}, q) - E(\text{pure}) - \Sigma\, n_i\mu_i + q(E_v + E_F), \qquad \text{(Eqn. S1)}$$

where E(defect, q) and E(pure) is system's total energy of the impurity and the pure host supercell, respectively. n_i is the quantity of atoms added to (positive n_i), or taken from (negative n_i) the host supercell, μ_i is the chemical potential for each added or removed atom. E_F is the Fermi level, with respect to the valence band maximum (VBM) of the bulk materials[5]. The atom chemical potential, μ_i, depends on the experimental condition under which the material is grown. In this calculation, these values are obtained from corresponding bulk systems.

We investigate the energetic stability of antisites and vacancies in bulk PbTe and PbS. The calculated formation energies as a function of the Fermi level (E_F) are shown in **Figure. S4**. For PbTe, either antisites PbTe or vacancies V_Te have higher formation energies if one Te is taken from the system while V_Pb has the lowest formation energy relative to the other types of defects. For PbS, the formation energy of antisites are higher than that of vacancies, and V_Pb has the lowest formation energy. These calculated results suggest that the V_Pb acceptor in both PbTe and PbS is the most stable point defects, consistent with the experimental observations in which Pb volatilization may give rise to the formation of Pb vacancy, which explain the intrinsic p-type conductivity.

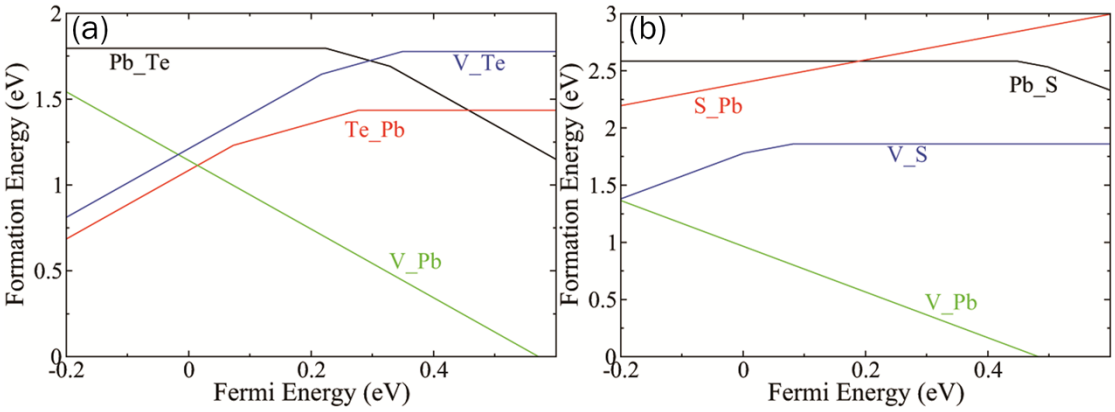

Figure S4 The Fermi level E_F dependent formation energies for various points defects in PbTe (a) and PbS (b). Kinks in the curves indicate transitions between different charge states.

Lattice thermal conductivity calculations

A modified Callaway model[6] is herein adopted to calculate the lattice thermal conductivity of this PbTe-PbS system. In the calculation, the system was deemed as a two-phase composite of PbTe-rich matrix and PbS-rich second phase; the contribution of each was evaluated by the corresponding volume fraction. The grain boundary scattering is believed negligible in our case, since TEM and SEM images exhibit the relatively too large grains (>2~3 μm) in PbTe-PbS composites. Moreover, strain and dislocations scattering are not considered, especially if the precipitations are endotaxial or semi-endotaxial. This is partly due to their incapability of impeding short and intermediate phonons which dominate the thermal transport, and partly can be ascribed to their insufficient number densities. In our calculations, only the intrinsic Umklapp and Normal processes, together with alloy scattering as well as precipitates scattering are included. Their individual contribution to the total relaxation time is listed as follows:

Umklapp process[7] $$\tau_U^{-1} \approx \frac{\hbar\gamma^2}{M\upsilon^2\theta_D}\varpi^2 T\exp(-\frac{\theta_D}{3T})$$ (Eqn. S2)

Normal process[6] $$\tau_N^{-1} \approx \beta\tau_U^{-1}$$ (Eqn. S3)

Alloy scattering[8,9] $\tau_D^{-1} = \frac{\varpi^4 \delta^3}{4\pi \upsilon^3} x(1-x)[(\Delta M / M)^2 + \varepsilon(\Delta\delta / \delta)^2]$ (Eqn. S4)

Precipitates scattering[10,11] $\tau_P^{-1} = v(\sigma_l^{-1} + \sigma_s^{-1})^{-1} V_P$ (Eqn. S5)

where the scattering cross-section in short- and long- wavelength regimes are $\sigma_S = 2\pi R^2$ and $\sigma_l = \frac{4}{9}\pi R^2 (\Delta D / D)^2 (\varpi R / \upsilon)^4$, respectively; D and ΔD are the mass density of host and density difference between host and nano-particles; V_P is the number density of nano-scale particle phases. Note: γ is the *Grüneisen* parameter, M is the molar mass, *v* is the average phonon group velocity, θ_D is the Debye temperature, β is a fitting parameter for Normal process, δ is the radius of impurity atom in host matrix, *x* is the ratio of point defects, Δ*M* is the mass difference between impurity and host atoms, ε is a phenomenological factor as a function of *Grüneisen parameter*. The effective lattice thermal conductivities in 20% and 30% PbS SPS samples were calculated as a combination of PbTe-rich matrix and PbS-rich nano-particles; the detailed method can be found elsewhere[12-14].

Table S1 The parameters used in our lattice thermal conductivity calculations can be found in other literatures[6,15].

PbTe		PbS	
θ_D	136 K	θ_D	145 K
γ	1.96	γ	2.52
M	334.8 g mol^{-1}	M	239.3 g mol^{-1}
v	1770 m s^{-1}	*v*	2040 m s^{-1}
β	2.5	β	0.8
δ_Te	0.221 *nm*	δ_S	0.184 *nm*
ε	65	ε	65
D	8.242 g cm^{-3}	D	7.597 g cm^{-3}

Electrical transport calculations

The calculations of electrical transport are performed based on Boltzmann Transport Equation (BTE) and energy-dependent relaxation time assumption in the framework of the 3-band Kane

model discussed elsewhere[16] and also in our previous works,[17,18] considering the contributions from light L band, heavy Σ band and conduction C band; meanwhile, the band non-parabolicity is taken into account using Kane E-k relation,[19,20] for large Fermi surface metals or at the band edge of highly degenerated semiconductors. The calculations were conducted in a simplified model where the system was taken as a PbTe-rich matrix with S point defects and PbS-rich precipitates. The dominant scattering mechanism is assumed to be acoustic phonon scattering[20,21] with a relaxation time τ_{ac}, while the contributions from point defects and precipitates scatterings are treated as perturbation terms and incorporated into the total relaxation time following *Matthiessen*'s rule as:

$$\tau = (\tau_{ac}^{-1} \ \tau_{d}^{-1} \ \tau_{p}^{-1})^{-1} \qquad \text{(Eqn. S6)}$$

where relaxation time of acoustic deformation potential phonon scattering[17]

$$\tau_{ac}^{-1}(\varepsilon) = (\varepsilon + \alpha\varepsilon^2)^{r}(1+2\alpha\varepsilon)^{-1}\frac{2\pi\hbar^4 C_l}{\Xi_{ac}^2(2m_{d1}^* k_B T)^{3/2}[(1-A)^2 - B]} \qquad \text{(Eqn. S7)}$$

relaxation time of point defect scattering[22,23]

$$\tau_{d}^{-1} = \frac{8\hbar^4}{3\sqrt{2}\pi\Omega x(1-x)\Delta^2 m_{d1}^{*3/2}(k_B T)^{1/2}}(\varepsilon+\alpha\varepsilon^2)^{-1/2}(1+2\alpha\varepsilon)^{-1}\left[1-\frac{8\alpha(\varepsilon+\alpha\varepsilon^2)}{3(1+2\alpha\varepsilon)^2}\right]^{-1} \qquad \text{(Eqn. S8)}$$

relaxation time due to precipitates scattering

$$\tau_{p}^{-1} = (1+\alpha\varepsilon)^{3/2}(1+2\alpha\varepsilon)^{-1}\varepsilon^{3/2}(2m_{d1}^* k_B T)^{3/2}\frac{2RC_B}{m_{d1}^*\phi V_0^2} \qquad \text{(Eqn. S9)}$$

Note: $\varepsilon = E/k_B T$, $\varepsilon_F = E_F/k_B T$ are reduced charge carrier energy and Fermi energy, the value of $\alpha = k_B T/E_g$ represents the band's non-parabolic feature, $m_d^* = N_v^{2/3} m_{d1}^*$ is the density-of-states mass in each band, where N_v is the degeneracy of the band and $m_{d1}^* = (m_l m_t^2)^{1/3}$ the effective mass of each single valley with m_l and m_t as effective masses along the longitudinal and transversal

directions respectively. f_0 is the Fermi-Dirac distribution function. The scattering parameter r=-1/2 when acoustic phonon scattering dominates. C_l is the combined elastic modulus, A and B are expressions defined in our previous work[17]. x is the ratio of point defects, Ω is the volume per atom, Δ is the alloy scattering potential. R is the average radius of precipitates, C_B is the so-called Born factor, Φ is the volume fraction of precipitates, V_0 is the interfacial potential between precipitates and matrix.

The total electrical transport properties come from the contributions from each band (L valence band, Σ valence band and C conduction band), expressed as:

$$\sigma=\sigma_L+\sigma_\Sigma+\sigma_C \quad \text{(Eqn. S10)}$$

$$S=\frac{S_L\sigma_L+S_\Sigma\sigma_\Sigma+S_C\sigma_C}{\sigma} \quad \text{(Eqn. S11)}$$

Table S2 The parameters used in the calculations come mostly from literatures,[16,19,20,24] PbTe is deemed as main matrix, the dopant Na and part of S as point defects with the other S as PbS precipitates.

m_C^*(C band)	0.3 m_0	Ξ_{ac} (C band)	22 eV
m_L^*(L band)	0.36 m_0	Ξ_{ac} (L band)	22 eV
m_Σ^*(Σ band)	2.1 m_0	Ξ_{ac} (Σ band)	17 eV
$E_{C\text{-}L}$	0.21+0.00045T (eV)	C_l (C, L and Σ band)	77 GPa
$E_{C\text{-}\Sigma}$	0.5 eV	Δ	2.5 eV
C_B	0.25	V_0	0.1 eV
a_0 (PbTe)	0.646 nm	a_0 (PbS)	0.594 nm

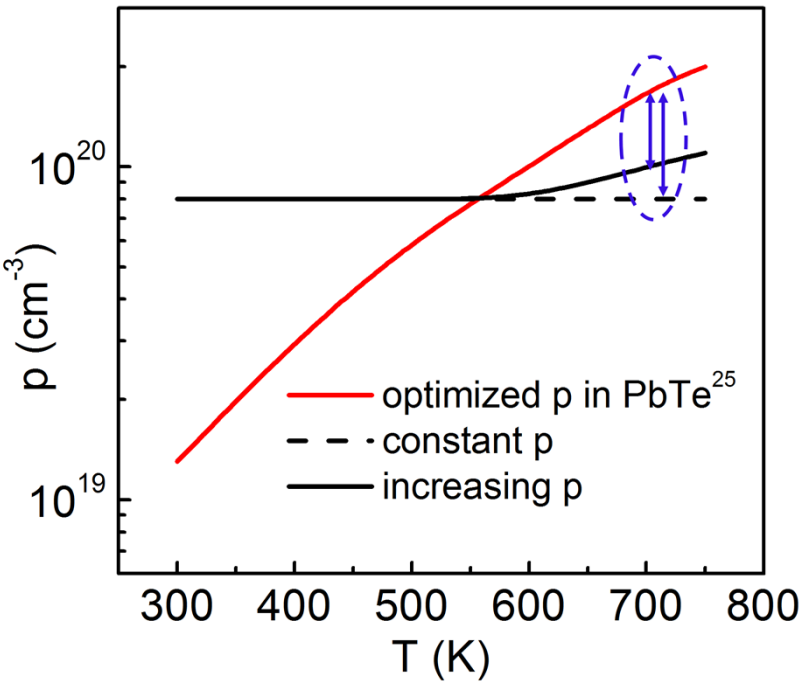

Figure S5 The gradually increasing hole concentration at elevated temperatures approaches the theoretical optimized concentration[25] in p-type PbTe, thus promising a superior thermoelectric performance.

Reference

(1) Perdew, J. P.; Wang, Y. *Physical Review B* **1992**, *45*, 13244.

(2) Kresse, G. *Phys. Rev. B* **1996**, *54*, 11.

(3) Kresse, G.; Joubert, D. *Physical Review B* **1999**, *59*, 1758.

(4) Blöchl, P. E. *Physical Review B* **1994**, *50*, 17953.

(5) Van de Walle, C. G.; Neugebauer, J. *Journal of Applied Physics* **2004**, *95*, 3851.

(6) He, J.; Girard, S. N.; Kanatzidis, M. G.; Dravid, V. P. *Advanced Functional Materials* **2010**, *20*, 764.

(7) Morelli, D.; Heremans, J.; Slack, G. *Physical Review B* **2002**, *66*.

(8) Yang, J.; Meisner, G.; Chen, L. *Applied physics letters* **2004**, *85*, 1140.

(9) Abeles, B. *Physical Review* **1963**, *131*, 1906.

(10) Kim, W.; Majumdar, A. *Journal of Applied Physics* **2006**, *99*, 084306.

(11) Mingo, N.; Hauser, D.; Kobayashi, N. P.; Plissonnier, M.; Shakouri, A. *Nano letters* **2009**, *9*, 711.

(12) Minnich, A.; Chen, G. *Applied Physics Letters* **2007**, *91*, 073105.

(13) Poon, S. J.; Petersen, A. S.; Wu, D. *Applied Physics Letters* **2013**, *102*, 173110.

(14) Wu, D.; Petersen, A. S.; Poon, S. J. *AIP Advances* **2013**, *3*, 082116.

(15) He, J.; Zhao, L. D.; Zheng, J. C.; Doak, J. W.; Wu, H.; Wang, H. Q.; Lee, Y.; Wolverton, C.; Kanatzidis, M. G.; Dravid, V. P. *Journal of the American Chemical Society* **2013**, *135*, 4624.

(16) Pei, Y.; Shi, X.; LaLonde, A.; Wang, H.; Chen, L.; Snyder, G. J. *Nature* **2011**, *473*, 66.

(17) Wu, D.; Zhao, L. D.; Hao, S.; Jiang, Q.; Zheng, F.; Doak, J. W.; Wu, H.; Chi, H.; Gelbstein, Y.; Uher, C.; Wolverton, C.; Kanatzidis, M.; He, J. *Journal of the American Chemical Society* **2014**, *136*, 11412.

(18) Wu, H. J.; Zhao, L. D.; Zheng, F. S.; Wu, D.; Pei, Y. L.; Tong, X.; Kanatzidis, M. G.; He, J. Q. *Nature communications* **2014**, *5*, 4515.

(19) Ravich, Y. I. *Semiconducting Lead Chalcogenides (Plenum)*. 1970.

(20) Faleev, S.; Léonard, F. *Physical Review B* **2008**, *77*.

(21) Pei, Y.; Wang, H.; Snyder, G. J. *Advanced materials* **2012**, *24*, 6125.

(22) Hauser, J. R.; Littlejohn, M. A.; Glisson, T. H. *Applied Physics Letters* **1976**, *28*, 458.

(23) Wang, H.; Wang, J.; Cao, X.; Snyder, G. J. *Journal of Materials Chemistry A* **2014**, *2*, 3169.

(24) Wang, H.; Schechtel, E.; Pei, Y.; Snyder, G. J. *Advanced Energy Materials* **2013**, *3*, 488.

(25) Pei, Y.; LaLonde, A. D.; Heinz, N. A.; Shi, X.; Iwanaga, S.; Wang, H.; Chen, L.; Snyder, G. J. *Advanced materials* **2011**, *23*, 5674.